

Calculation and Analysis of an Analytical Model for Magnetic Field Monitoring Based on TREE in Eddy Current Testing

Feng Jiang^{1,2} and Shulin Liu¹

¹ School of Mechatronics Engineering and Automation
Shanghai University, Shanghai, 200072, China
lsl346@shu.edu.cn

² School of Mechatronics Engineering
Jiangsu College of Information Technology, Wuxi, 214153, China
jiangf@jsit.edu.cn

Abstract — In this work, theoretical model for magnetic field monitoring rather than traditional detection of coil impedance is investigated and analyzed. The truncated region eigenfunction expansion (TREE) method [1] offers analytical expressions by truncating the solution region to a finite length, so magnetic field can be derived in a series of proper eigenfunctions instead of the integral form, as it traditionally happens. The influences of truncation interval h , the number of summation n and excitation current frequency f on magnetic field above conductive plate for the model accuracy are estimated. The comparison of the results obtained between theoretical calculation and the finite element method shows excellent agreement under certain conditions. An applicative example is presented to assess the proposed theory to different conductor problem using the eddy current field derived by the analytical solution. The analytical model can be beneficial for analysis, parametric studies and development of eddy current testing system.

Index Terms — Analytical model, eddy current testing, finite element method, magnetic field.

I. INTRODUCTION

The eddy current testing (ECT) has been used for a wide variety of applications such as the detection of cracks and residual stresses, measurement of coating or metal thickness, determination of the alloy composition and hardness of tested object and so on [2-8]. Previous work has mainly focused on practical applications such as crack detection using the various types of coil and the exciting current [9,10]. In contrast, there are relatively few literature reports on theoretical and behavioural modeling. Modeling is a powerful tool for design optimization, enhancing a better understanding of the relevant physics and improving the reliability of defect analysis.

ECT can be studied by applying the electric circuit theory and the electromagnetic field theory [11-14]. However, electric circuit method is only approximate and it predicts signals that differ greatly from the measured signals. It is more suitable for analysis to use electromagnetic field theory. The electromagnetic field can be solved by analytical method or numerical method. Now, the numerical method such as the finite element method is widely used to predict signals in ECT [15-17]. The analytical method is more advantageous to obtain the general solution in the form of closed mathematical expression and need fewer computation resources as well as a useful starting point for some numerical optimization. So the analytical solution makes it possible to solve the inverse problem where the unknown geometric shape of a defect is to be reconstructed [18,19]. Moreover, analytical solution can easily be used for quantitative analysis, parametric estimation and calibration of the measurement device. Dodd and Deeds [20] proposed the “closed-form” solution for two different geometries: a rectangular cross-section coil above a plane and a rectangular cross-section coil encircling a two-conductor rod. The solutions were given in terms of integrals of Bessel functions. Measured values of coil impedance have been compared with calculated values and they have shown excellent agreement. On the basis of previous achievements made by Dodd and Deeds in analytical modeling, the TREE method has been employed to express magnetic vector potential as a series of proper eigenfunctions by truncating the domain of the problem instead of the integral form, as it traditionally happens [1]. As for the author’s knowledge, until now, the TREE method has been successfully employed only for prediction of coil impedance to a conductive plate with a cylindrical hole or a slot, conductive wedge and so on [21-23].

All eddy current problems above are usually detected as an impedance change of the pick coil [24,25].

The sensitivity of pick coil is reduced in detecting deep buried flaws because of low excitation frequency. Thus, it is more beneficial to measure the magnetic field rather than coil impedance variation. Magnetic field sensors based on Hall effect, giant magnetoresistance effect or superconducting quantum interference device have been used for ECT successfully [26,27]. Unfortunately, in this case, the measured signals from magnetic field sensors needed to be verified by theoretical methods. If compared with experimental studies, only a few theoretical analyses were conducted for magnetic field detecting in ECT.

In this paper, we extend the TREE method to the magnetic flux density, rather than the coil impedance. The formulas of two-dimensional magnetic field including source field and eddy current field above the conductor surface are deduced. Then, efforts have been made to determine the optimal value for the parameters that appear in equations.

II. SECTION ANALYTICAL MODELING

A. Formulation of magnetic vector potential

The mathematical model for eddy current problem at low frequencies is described by Maxwell's equations. Maxwell's equations in differential form are:

$$\begin{cases} \nabla \times \mathbf{H} = \mathbf{J} + \frac{\partial \mathbf{D}}{\partial t} \\ \nabla \times \mathbf{E} = -\frac{\partial \mathbf{B}}{\partial t} \\ \nabla \cdot \mathbf{D} = \rho \\ \nabla \cdot \mathbf{B} = 0 \end{cases}, \quad (1)$$

where some quantities above are defined as: \mathbf{H} -the magnetic field intensity, \mathbf{J} -the current density, \mathbf{D} -the electric flux density, \mathbf{E} -the electric field intensity, \mathbf{B} -the magnetic flux density, ρ -the volume electric charge density. The additional relations are the material constitutes relations:

$$\begin{cases} \mathbf{D} = \varepsilon \mathbf{E} \\ \mathbf{B} = \mu \mathbf{H} \\ \mathbf{J} = \sigma \mathbf{E} \end{cases}, \quad (2)$$

where ε is the permittivity, μ is the magnetic permeability, σ is the electric conductivity.

Excitation frequency is low and consequently the displacement current is neglected. Since the displacement currents can be neglected and sinusoidal excitation current is assumed, Maxwell's equations can be rewritten as follows:

$$\begin{cases} \nabla \times \mathbf{H} = \mathbf{J}_s + \mathbf{J}_e \\ \nabla \times \mathbf{E} = -j\omega \mathbf{B} \\ \nabla \cdot \mathbf{D} = \rho \\ \nabla \cdot \mathbf{B} = 0 \end{cases}. \quad (3)$$

The current densities given in Eq. (3) include source current density \mathbf{J}_s and eddy current density \mathbf{J}_e . In order

to simplify the equations for calculation, the magnetic vector potential \mathbf{A} is defined as $\nabla \times \mathbf{A} = \mathbf{B}$ with provision for $\nabla \cdot \mathbf{A} = 0$. The electric scalar ϕ is defined as $-\nabla \phi = \mathbf{E} + j\omega \mathbf{A}$. Substituting these definitions above into Eq. (3), we will have:

$$\nabla^2 \mathbf{A} = -\mu \mathbf{J}_s + \mu (\nabla \phi + j\omega \mathbf{A}). \quad (4)$$

Combined with Eq. (1) and definition of ϕ , the other equation can be obtained:

$$\nabla \cdot (\nabla \phi + j\omega \mathbf{A}) = 0. \quad (5)$$

We consider a cylindrical coil with rectangular cross-section, placed above a conductive plate. The dimension of conductive plate is assumed big enough compared to the size of coil. The axisymmetric model is shown in Fig. 1. The region above conductive plate is region 0 and conductive plate is region 1. The coil is assumed to be air-cored with N turns, inner radius r_1 , outer radius r_2 , thickness $z_2 - z_1$. The distance z_1 is called "lift-off". The coil is excited by a sinusoidal current of angular frequency ω .

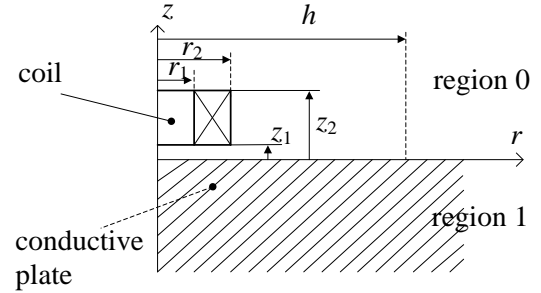


Fig. 1. 2D axisymmetric view of model.

We use cylindrical coordinates in solving the problem due to the axial symmetry. Then the magnetic vector potential A has only circumferential component as a function of r and z . Thus, the Eq. (5) is identically satisfied and the Eq. (4) can be simplified into:

$$\frac{\partial^2 A}{\partial r^2} + \frac{1}{r} \frac{\partial A}{\partial r} + \frac{\partial^2 A}{\partial z^2} - \frac{A}{r^2} = -\mu J_s + k^2 A, \quad (6)$$

where $k^2 = j\omega\mu\sigma$.

B. Integral solution of the magnetic vector potential

Equation (6) can be solved by the separation of variables and the general solution has the following form [20]:

$$A(r, z) = \int_0^\infty [A(\alpha)J_1(\alpha r) + B(\alpha)Y_1(\alpha r)] \times [C(\alpha)e^{\lambda z} + D(\alpha)e^{-\lambda z}] d\alpha, \quad (7)$$

where $\lambda = \sqrt{\alpha^2 + k^2}$. J_1 denotes the Bessel function of the first kind and first order. Y_1 denotes the Bessel function of the second kind and first order. A , B , C and D are unknown coefficients.

Because the function Y_1 tends to infinity, we set

$B(\alpha) = 0$. The potential in the air ($k = 0$) below the coil assumes the following expression:

$$A_0(r, z) = \int_0^{\infty} J_1(\alpha r) [C_s e^{\alpha z} + D_{ec} e^{-\alpha z}] d\alpha. \quad (8)$$

Moreover, in order to remain finite of the potential, we set $D(\alpha) = 0$ in region 1. Thus, the potential in the conductive plate assumes the following expression:

$$A_1(r, z) = \int_0^{\infty} J_1(\alpha r) C_1(\alpha) e^{\lambda z} d\alpha. \quad (9)$$

The unknown coefficients in Eqs. (8) and (9) are determined by imposing the interface conditions between the two regions:

$$\left. \begin{aligned} A_0 &= A_1 \\ \frac{\partial A_0}{\partial z} &= \frac{1}{\mu_r} \frac{\partial A_1}{\partial z} \end{aligned} \right|_{z=0}. \quad (10)$$

After substituting Eqs. (8) and (9) into Eq. (10) we get the equations for the two unknown coefficients:

$$\left\{ \begin{aligned} C_1 &= C_s \frac{2\alpha\mu_r}{\alpha\mu_r + \lambda} \\ D_{ec} &= C_s \frac{\alpha\mu_r - \lambda}{\alpha\mu_r + \lambda} \end{aligned} \right. \quad (11)$$

The term C_s is a source coefficient which has a form:

$$C_s = \frac{\mu_0 i}{2} \frac{\chi(\alpha r_1, \alpha r_2)}{\alpha^3} (e^{-\alpha z_1} - e^{-\alpha z_2}), \quad (12)$$

where $i = NI / [(r_2 - r_1)(z_2 - z_1)]$ is the source current density of the coil. The term $\chi(\alpha r_1, \alpha r_2)$ can be expressed as follows [20]:

$$\chi(x_1, x_2) = \int_{x_1}^{x_2} x J_1(x) dx. \quad (13)$$

Thus, we obtain the integral expression for the potential in the air below the coil:

$$\begin{aligned} A_0(r, z) &= \frac{\mu_0 i}{2} \int_0^{\infty} J_1(\alpha r) e^{\alpha z} \frac{\chi(\alpha r_1, \alpha r_2)}{\alpha^3} (e^{-\alpha z_1} - e^{-\alpha z_2}) d\alpha \\ &+ \frac{\mu_0 i}{2} \int_0^{\infty} J_1(\alpha r) e^{-\alpha z} \frac{\chi(\alpha r_1, \alpha r_2)}{\alpha^3} (e^{-\alpha z_1} - e^{-\alpha z_2}) \frac{\alpha\mu_r - \lambda}{\alpha\mu_r + \lambda} d\alpha, \quad (14) \\ &= A^s + A^e \end{aligned}$$

where A^s stands for the source potential, A^e corresponds to the one due to the eddy current.

C. Analytical solution of magnetic flux density

Equation (14) has been derived by assuming an infinite solution region. In the TREE method, the solution region is assumed finite in the radial direction ($0 \leq r \leq h$). Following the separation of variables and the imposition of Dirichlet boundary condition at $r = h$, the general expression for the magnetic vector potential in region 0 is given as [1]:

$$A_0(r, z) = \sum_{i=1}^{\infty} J_1(\alpha_i r) (C_i e^{\alpha_i z} + D_i e^{-\alpha_i z}). \quad (15)$$

The term C_i is a source coefficient which has a form [1]:

$$C_i = \mu_0 i \frac{\chi(\alpha_i r_1, \alpha_i r_2)}{\alpha_i^4 [hJ_0(\alpha_i h)]^2} (e^{-\alpha_i z_1} - e^{-\alpha_i z_2}). \quad (16)$$

The coefficient D_i is calculated using the same method as D_{ec} above. Thus the potential can be expressed as follow:

$$\begin{aligned} A_0(r, z) &= \mu_0 i \sum_{i=1}^{\infty} [J_1(\alpha_i r) e^{\alpha_i z} \frac{\chi(\alpha_i r_1, \alpha_i r_2)}{\alpha_i^4 [hJ_0(\alpha_i h)]^2} (e^{-\alpha_i z_1} - e^{-\alpha_i z_2}) + \\ &J_1(\alpha_i r) e^{-\alpha_i z} \frac{\chi(\alpha_i r_1, \alpha_i r_2)}{\alpha_i^4 [hJ_0(\alpha_i h)]^2} (e^{-\alpha_i z_1} - e^{-\alpha_i z_2}) \frac{\alpha_i \mu_r - \lambda_i}{\alpha_i \mu_r + \lambda_i}] \end{aligned} \quad (17)$$

Once the potential is calculated, the magnetic flux density can be derived from:

$$B = -\frac{\partial A}{\partial z} \mathbf{r}_0 + \frac{1}{r} \frac{\partial (rA)}{\partial r} \mathbf{z}_0. \quad (18)$$

Substituting the Eq. (17) into Eq. (18), we will have:

$$\begin{aligned} B_0(r, z) &= \mu_0 i \sum_{i=1}^{\infty} \left[J_1(\alpha_i r) \left(-e^{\alpha_i z} + e^{-\alpha_i z} \frac{\alpha_i \mu_r - \lambda_i}{\alpha_i \mu_r + \lambda_i} \right) \frac{\chi(\alpha_i r_1, \alpha_i r_2)}{\alpha_i^3 [hJ_0(\alpha_i h)]^2} (e^{-\alpha_i z_1} - e^{-\alpha_i z_2}) \right] \mathbf{r}_0 \\ &+ \mu_0 i \sum_{i=1}^{\infty} \left[J_0(\alpha_i r) \left(e^{\alpha_i z} + e^{-\alpha_i z} \frac{\alpha_i \mu_r - \lambda_i}{\alpha_i \mu_r + \lambda_i} \right) \frac{\chi(\alpha_i r_1, \alpha_i r_2)}{\alpha_i^3 [hJ_0(\alpha_i h)]^2} (e^{-\alpha_i z_1} - e^{-\alpha_i z_2}) \right] \mathbf{z}_0 \end{aligned} \quad (19)$$

Finally, we have the analytical expressions of magnetic flux density at $0 \leq z \leq z_1$:

$$\left\{ \begin{aligned} B_0(r) &= \mu_0 i \sum_{i=1}^{\infty} J_1(\alpha_i r) \left(-e^{\alpha_i z} \right) \frac{\chi(\alpha_i r_1, \alpha_i r_2)}{\alpha_i^3 [hJ_0(\alpha_i h)]^2} (e^{-\alpha_i z_1} - e^{-\alpha_i z_2}) \\ \Delta B_0(r) &= \mu_0 i \sum_{i=1}^{\infty} J_1(\alpha_i r) \left(e^{-\alpha_i z} \frac{\alpha_i \mu_r - \lambda_i}{\alpha_i \mu_r + \lambda_i} \right) \frac{\chi(\alpha_i r_1, \alpha_i r_2)}{\alpha_i^3 [hJ_0(\alpha_i h)]^2} (e^{-\alpha_i z_1} - e^{-\alpha_i z_2}) \\ B_0(z) &= \mu_0 i \sum_{i=1}^{\infty} J_0(\alpha_i r) \left(e^{\alpha_i z} \right) \frac{\chi(\alpha_i r_1, \alpha_i r_2)}{\alpha_i^3 [hJ_0(\alpha_i h)]^2} (e^{-\alpha_i z_1} - e^{-\alpha_i z_2}) \\ \Delta B_0(z) &= \mu_0 i \sum_{i=1}^{\infty} J_0(\alpha_i r) \left(e^{-\alpha_i z} \frac{\alpha_i \mu_r - \lambda_i}{\alpha_i \mu_r + \lambda_i} \right) \frac{\chi(\alpha_i r_1, \alpha_i r_2)}{\alpha_i^3 [hJ_0(\alpha_i h)]^2} (e^{-\alpha_i z_1} - e^{-\alpha_i z_2}) \end{aligned} \right. \quad (20)$$

where the eigenvalues of α_i are the positive roots of $J_1(\alpha_i h) = 0$. $B_0(r)$ and $B_0(z)$ represent the radial and axial magnetic field, respectively, above the conductive plate generated by the excitation coil. $\Delta B_0(r)$ and $\Delta B_0(z)$ respectively stand for the radial and axial magnetic field caused by eddy current. We can get accurate solution of magnetic field easily using several summation operations from Eq. (20).

III. FE MODELING

We will obtain the magnetic field distributions using ANSOFT Maxwell [28] to verify the analytical model above. ANSOFT Maxwell is a finite element analysis software that can automatically adjust areas of the finite element mesh exhibiting large errors. Table 1 shows the main dimensions of the coil and conductive plate. The parameters L and T in Table 1 represent the length and

thickness of conductive plate respectively. The 2D model is shown below using the 2D RZ axisymmetric solver. Coils are wound with copper enameled wires, belonging to the stranded wires. The amplitude of the sinusoidal excitation current is 40 ampere-turns and its phase is 0 degree. Boundary conditions are balloon (upper and lower boundary), symmetry (left boundary) and vector potential = 0 (right boundary) respectively. The excitation current frequency is set at 1 kHz.

Table 1: Coil and conductive plate parameters

Coil	Conductive Plate
$r_1 = 2 \text{ mm}$	$\sigma = 3.6 \times 10^7 \text{ S/m}$
$r_2 = 4 \text{ mm}$	$\mu_r = 1$
$z_2 - z_1 = 3 \text{ mm}$	$L = 160 \text{ mm}$
$z_1 = 1 \text{ mm}$	$T = 20 \text{ mm}$
$N = 800$	

The distribution cloud of magnetic field intensity is shown in Fig. 2 through the analysis of model above. Figure 3 is the distribution of magnetic field lines. As the figures show, the magnetic flux density of the coil is close to the maximum and the lines are crowded together. Inside the conductor, magnetic field near the surface of the detection coil is strong. This shows that eddy current is concentrated in the surface and near the surface of the conductor.

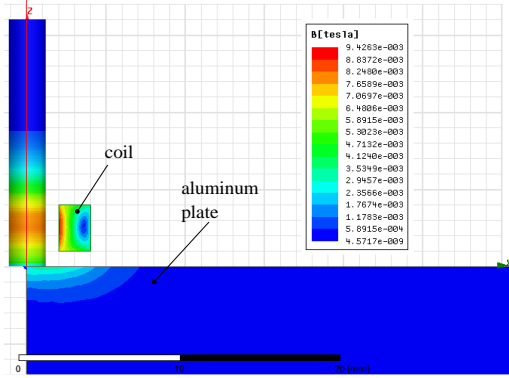


Fig. 2. 2D simulation model and distribution cloud of magnetic field intensity.

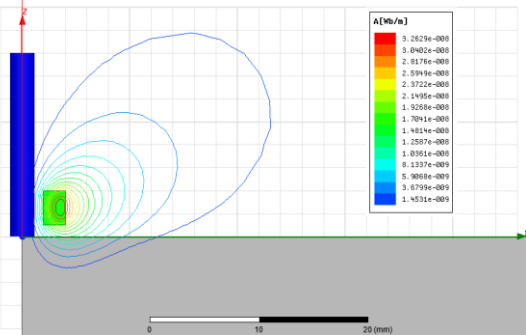


Fig. 3. Distribution of magnetic field lines.

IV. ANALYSIS AND DISCUSSION

A. Effects of the length of the truncation interval h

We compute magnetic field between the conductor and coil and show how the modeling error is influenced by the length of the truncation interval h . We choose $h = r_2, h = 20r_2, h = 40r_2, h = 80r_2$ respectively and the number of the summation $n = 50$.

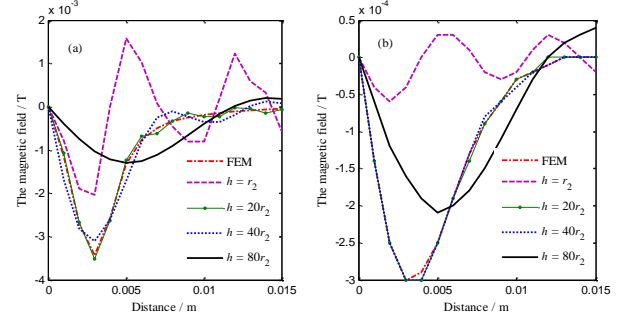


Fig. 4. (a) The real part and (b) imaginary part of radial magnetic field as a function of distance under different truncation interval at $z = 0.5 \text{ mm}$.

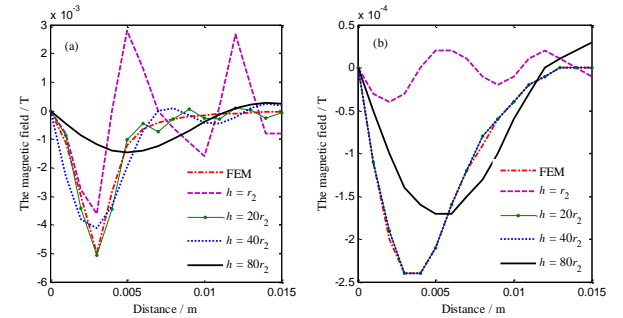


Fig. 5. (a) The real part and (b) imaginary part of radial magnetic field as a function of distance under different truncation interval at $z = 1 \text{ mm}$.

Figures 4 (a), 4 (b) show the real and imaginary parts of radial magnetic field calculated at $z = 0.5 \text{ mm}$ respectively. The real part and imaginary part of radial magnetic field calculated at $z = 1 \text{ mm}$ are shown in Figs. 5 (a) and 5 (b) respectively. Compared with finite element analysis, the results can be found from figures as follows: (1) The fact is not that h value is the bigger the better as theoretical analysis. Its impact on the calculation result is very large and h value cannot be too large or too small. Hence, the value of h should be in a certain range. Calculation results can infinitely approach the simulation results by selecting the appropriate h value. It proves that the eddy current concentrates only in a very narrow area. This is physically consistent because the electromagnetic field does not extend to great distance from the excitation coil. Therefore, the value of h is chosen only in relation to the outer radius

of the coil. (2) The calculated values fluctuate greatly when $0 < h < 2r_2$. Results have no obvious regularity, so we do not recommend h value within this range. With the increase of the value of h , the error increases slightly when $2r_2 \leq h \leq 40r_2$. As the error can be maintained within 10%, the calculation results can basically reflect the magnetic field distribution. The error is only 0.87% at $r = 3$ mm when $h = 2r_2$. Table 2 lists the calculation results at $h = 5r_2$, $h = 10r_2$, $h = 15r_2$ and simulation results at $z = 0.5$ mm. It can be seen that error is very small within this range. The difference between the calculated results and the simulation results becomes larger when $h \geq 40r_2$. The error is 70% at $r = 3$ mm when $h = 80r_2$. Therefore, too large h values will cause larger error obviously. It is not recommended to adopt the h value in the range of $h \geq 40r_2$ (3) The results also show that the real and imaginary part of radial magnetic field reaches the maximum at $r = 3$ mm which is the center of the coil width. The radial magnetic field is zero at $r = 0$ mm and $r > 15$ mm. These results are in accord with what we expected completely.

Table 2: Calculated and simulated results as a function of distance under different truncation interval (unit: 10^{-5} T)

	FEM		$h = 5r_2$		$h = 10r_2$		$h = 15r_2$	
	Re	Im	Re	Im	Re	Im	Re	Im
0	0	0	0	0	0	0	0	0
1	-116	-14	-116	-14	-115	-14	-110	-14
2	-269	-25	-271	-25	-270	-25	-274	-25
3	-344	-30	-351	-30	-353	-30	-350	-30
4	-258	-29	-255	-30	-254	-30	-256	-30
5	-132	-25	-131	-25	-131	-25	-131	-25
6	-76	-19	-76	-19	-76	-19	-75	-19
7	-49	-13	-49	-14	-49	-14	-51	-14
8	-34	-9	-34	-9	-34	-9	-33	-9
9	-25	-6	-24	-5	-25	-6	-26	-6
10	-19	-3	-18	-3	-18	-3	-18	-3

B. Effects of the number of summation n

It is expected that the greater the number of summation should be, the greater the ability to approximate a real result. To validate this presumption, the calculation results are shown in Fig. 6 for $n = 5, 10, 80, 200$ and 1000 keeping $z = 0.5$ mm and $h = 5r_2$. Figures 6 (a) and 6 (b) are the real part and imaginary part of radial magnetic field respectively.

It is easy to see that the results are quite different from our presumption. (1) When $n \geq 10$, it can basically meet the requirements with the error $< 5\%$ (at the point of maximum radial magnetic field). This is a strong proof of the biggest advantage for this mathematical model, that is, it can replace the theoretical needs of infinite summation through several summation operations, eliminating the need for the use of infinite integral calculation problem. (2) The number of summation is not the bigger the better as theoretical analysis. It is found that too many summation number results in lower

accuracy of the model. The calculation time will be very long at the same time. The error is 9.3% when $n = 1000$. The calculation time is about 70 seconds using Matlab. In contrast, the error is only 2.6% and the calculation time is only 3 seconds when $n = 20$. (3) The calculated data is also unstable when the number of summation is too large. The magnetic field presents abnormal increase as the distance is far enough. This does not conform to the actual situation obviously.

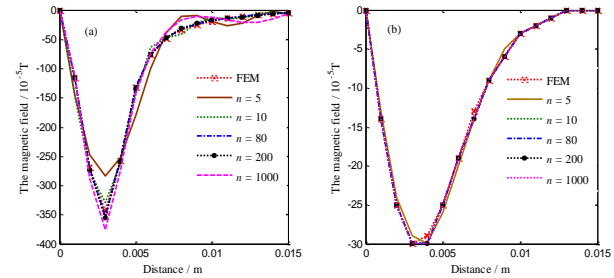


Fig. 6. (a) The real part and (b) imaginary part of radial magnetic field as a function of distance under different number of summation.

C. Effects of the excitation current frequency f

The excitation current frequency is a very important parameter in eddy current testing. Here we mainly analyze the error values of the radial magnetic field and the axial magnetic field calculated by the mathematical model under different frequencies compared with the simulation. The following frequencies are used: 50 Hz, 2 kHz, 10 kHz, 500 kHz, 1 MHz. According to the analysis results obtained above, we take $h = 5r_2$, $n = 20$. The magnitudes (real part and imaginary part) of the radial magnetic field B_r and the axial magnetic field B_z at $z = 0.5$ mm are calculated.

As shown in Fig. 7 (a), the error of $\text{Re}(B_r)$ decreases gradually as the frequency increases. The maximum error occurs at $r = 3$ mm when $f = 50$ Hz. The maximum error value is 9×10^{-5} T. In fact, the relative error is very small compared to the magnetic field value of 324×10^{-5} T at this time. Under the same frequency, the maximum error also occurs at $r = 3$ mm, because the magnetic field value is the largest. In Fig. 7 (b), the calculated values are in good agreement with the FEM values, except for very few points ($f = 50$ Hz, $r = 8$ mm; $f = 2$ kHz, $r = 3$ mm; $f = 500$ kHz, $r = 2$ mm). According to the further analysis, this error is not caused by the model itself. Since the imaginary part of the radical magnetic field is very small, the error is caused by data truncation during the calculation. Therefore, we believe that the calculation of the imaginary part of the radical magnetic field is consistent with the simulation results and the results are not affected by the frequency. The real part of the axial magnetic field is shown in Fig. 7 (c). The error occurs mainly at the starting position, especially $r = 0$. When

the frequency is less than or equal to 2 kHz, the error is obvious. The maximum error is 113×10^{-5} T with magnetic field of 517×10^{-5} T at $r = 0$ when $f = 2$ kHz. The error becomes very small at $r = 0$ when the frequency is greater than 2 kHz. Therefore, the error is greater only at a lower frequency and very close to zero point for the real part of the axial magnetic field. The imaginary part of the axial magnetic field is shown in Fig. 7 (d). The error is relatively large at $r = 0$ when $f = 2$ kHz. This result is similar to that obtained for the real part of the axial magnetic field. In the other frequency range, the calculation results are almost consistent with the simulation results.

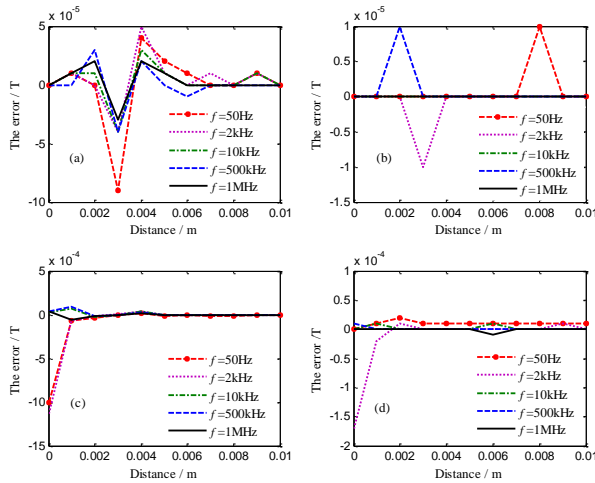


Fig. 7. Comparison of magnetic field between the calculation results and FEM under different frequencies. (a) The error of $\text{Re}(B_r)$; (b) the error of $\text{Im}(B_r)$; (c) the error of $\text{Re}(B_z)$; (d) the error of $\text{Im}(B_z)$.

In general, the results obtained by the mathematical model are not affected by the frequency. The model can maintain a high accuracy at any frequency. The error is smaller as the exciting current frequency increases. The larger frequency has no research value, because the skin depth is very small at this time and eddy current effect is not obvious.

V. APPLICATION

In this section we present an application example of the model to different conductor problems. Zinc and aluminum are widely used in the industrial field, and their integrity is very important for safety production. At present, their evaluation is mainly based on the principle of material conductivity change. In this section, zinc is first selected to analyze the distributions of source field and eddy current field. On this basis, zinc and aluminium are studied to analyze the eddy current field changes caused by different electrical conductivity. The electrical conductivities of zinc and aluminum are 1.86×10^7 S/m

and 3.6×10^7 S/m respectively. The relative permeability of both materials is approximately 1. We can only get the sum of the magnetic field using the finite element method which cannot distinguish between the source field generated by the excitation coil and the magnetic field caused by eddy current. But the two types of magnetic field can be clearly separated by Eq. (20). This is a very significant feature of the mathematical model distinguishing the finite element method.

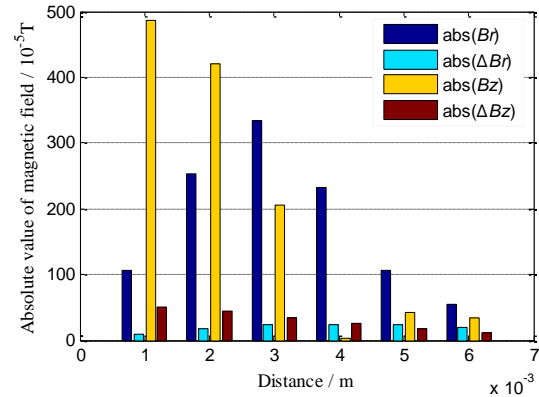


Fig. 8. The components of the magnetic field.

The components of the magnetic field are calculated for conductor zinc at $z = 0.5$ mm. The following values of the parameters are used: lift-off = 1 mm, $h = 5r_2$ and $n = 20$. According to the previous analysis, the error is 2.6% under these conditions. It can be seen from Fig. 8 that the radial and axial magnetic field above the conductor are greatly changed by eddy current. This is the basic principle that we adopt the magnetic sensor to measure the variation of magnetic field and realize the detection. From the height of the columns in Fig. 8, it is apparent that the magnetic field at different positions is not equal. The source field B_r and eddy current field ΔB_r increase firstly and then decrease with the increase of radial distance. The maximum B_r is 33.3 Gauss at $r = 3$ mm, which is the center of the coil width. The maximum ΔB_r is 2.4 Gauss at $r = 4$ mm, which is the outside radius of coil. The source field B_z and eddy current field ΔB_z are getting smaller and smaller with the increase of radial distance. The only difference is that source field B_z drops to zero suddenly at $r = 4$ mm. It is determined by the coil structure. In general, the changes of source field and eddy current field are similar with the increase of radius distance.

By means of the mathematical model, we can also analyze the magnetic field variations ΔB_r and ΔB_z caused by the conductivity or the permeability of detected object for eddy current nondestructive testing and thickness detection. The magnetic field variations ΔB_r and ΔB_z are calculated for the zinc and aluminum respectively in Fig. 9. It shows that the magnetic field

variations are very sensitive to the conductivity of the material being measured. This is a necessary precondition that we use the eddy current to detect cracks, corrosion and other defects. With the increase of conductivity of the material, the corresponding variation of the magnetic field increases. In general, the regularity of magnetic field variation caused by electrical conductivity is similar to that of magnetic field induced by eddy current.

According to Fig. 9, if we detect the magnetic field variations ΔBr , the maximum change of magnetic field variations $\Delta(\Delta Br)$ owing to the electrical conductivity takes place at $r = 3$ mm or $r = 4$ mm. If we detect the magnetic field variations ΔBz , the maximum change of magnetic field variations $\Delta(\Delta Bz)$ owing to the electrical conductivity takes place at $r = 0$ mm or $r = 1$ mm. That is to say, if sensitivity direction of sensor is radial, we can place the sensor at the outside radius of coil. If sensitivity direction of sensor is axial, we can place the sensor at the symmetry center of coil. The above analysis results have important implications for the arrangement of sensor position as well as to determine the sensitive direction of the magnetic sensor.

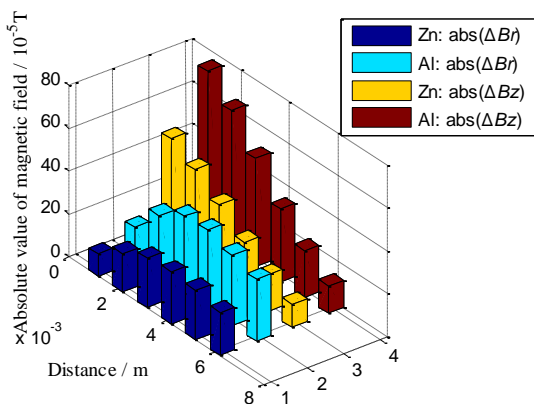


Fig. 9. Magnetic field variations for zinc and aluminum.

VI. CONCLUSION

(1) The analytical solution to mathematical model of eddy current problem is derived based on the magnetic field monitoring rather than traditional detection of coil impedance. The magnetic field can be decomposed into source field and eddy current field easily. This feature can be seen from an example of its application to different conductor problems.

(2) The value of the added distance for the computation, h , is not the bigger the better as theoretical analysis and should be in a certain range. The calculation results can infinitely approach the simulation results at $2r_2 \leq h \leq 40r_2$.

(3) It can basically meet the requirements that the error is less than 5% with the number of summation $n \geq 10$. There is no need to choose too many summation numbers as theoretical analysis. Not only does the error

increase correspondingly, but also the calculation time is very long. So we can only replace infinite summation or infinite integral calculation with several summation operations to obtain high accuracy.

(4) Model accuracy is almost not affected by the frequency. But it should be noticed that there is some error of the axial magnetic field for lower frequency at $r = 0$, which should be analyzed by further experiments.

ACKNOWLEDGMENT

This work was supported by the National Natural Science Foundation of China (51575331 and 51175316) and Shanghai Key Laboratory of Intelligent Manufacturing and Robotics (ZK1801).

REFERENCES

- [1] T. P. Theodoulidis and J. R. Bowler, "The truncated region eigenfunction expansion method for the solution of boundary value problems in eddy current nondestructive evaluation," *Review of Progress in Quantitative Nondestructive Evaluation*, Golden, Colorado, pp. 403-408, Apr. 2005.
- [2] A. Sophian, G. Tian, and M. Fan, "Pulsed eddy current non-destructive testing and evaluation: A review," *Chinese Journal of Mechanical Engineering*, vol. 30, no. 3, pp. 500-514, May 2017.
- [3] F. Jiang, S. L. Liu, and S. G. Xiao, "Quantitative estimation of rectangular surface crack based on the 2-D modeling of surface magnetic field with long straight rectangular wire," *IEEE Transactions on Magnetics*, vol. 54, no. 5, pp. 1-12, May 2018.
- [4] J. W. Wilson, G. Y. Tian, and S. Barrans, "Residual magnetic field sensing for stress measurement," *Sensors and Actuators A: Physical*, vol. 135, no. 2, pp. 381-387, Apr. 2007.
- [5] L. Yong, Z. Chen, Y. Mao, et al., "Quantitative evaluation of thermal barrier coating based on eddy current technique," *NDT & E International*, vol. 50, pp. 29-35, Sept. 2012.
- [6] M. S. Amiri and M. Kashefi, "Application of eddy current nondestructive method for determination of surface carbon content in carburized steels," *NDT & E International*, vol. 42, no. 7, pp. 618-621, Oct. 2009.
- [7] D. Mercier, J. Lesage, X. Decoopman, et al., "Eddy currents and hardness testing for evaluation of steel decarburizing," *NDT & E International*, vol. 39, no. 8, pp. 652-660, Dec. 2006.
- [8] B. Helifa, M. Féliachi, I. K. Lefkaier, et al., "Characterization of surface cracks using eddy current NDT simulation by 3D-FEM and inversion by neural network," *Applied Computational Electromagnetics Society Journal*, vol. 31, no. 2, pp. 187-194, Feb. 2016.
- [9] A. Sophian, G. Y. Tian, D. Taylor, et al., "Electromagnetic and eddy current NDT: A review," *Insight-*

- Non-Destructive Testing and Condition Monitoring*, vol. 43, no. 5, pp. 302-306, May 2001.
- [10] D. Rifai, A. N. Abdalla, K. Ali, et al., "Giant magnetoresistance sensors: A review on structures and non-destructive eddy current testing applications," *Sensors*, vol. 16, no. 3, pp. 1-30, Mar. 2016.
- [11] H. Ammari, A. Buffa, and J.-C. Nédélec, "A justification of eddy currents model for the maxwell equations," *SIAM Journal on Applied Mathematics*, vol. 60, no. 5, pp. 1805-1823, May 2000.
- [12] J. R. Nagel, "Fast finite-difference calculation of eddy currents in thin metal sheets," *Applied Computational Electromagnetics Society Journal*, vol. 33, no. 6, pp. 575-584, June 2018.
- [13] R. K. Murphy, H. A. Sabbagh, and E. H. Sabbagh, "A multiscale algorithm for eddy-current nondestructive evaluation based on volume-integral equations: Initial concepts," *Applied Computational Electromagnetics Society Journal*, vol. 31, no. 4, pp. 333-339, Apr. 2016.
- [14] C. Huang, X. Wu, Z. Xu, et al., "Ferromagnetic material pulsed eddy current testing signal modeling by equivalent multiple-coil-coupling approach," *NDT & E International*, vol. 44, no. 2, pp. 163-168, Mar. 2011.
- [15] H. Tsuboi, N. Seshima, I. Sebestyen, et al., "Transient eddy current analysis of pulsed eddy current testing by finite element method," *IEEE Transactions on Magnetics*, vol. 40, no. 2, pp. 1330-1333, Mar. 2004.
- [16] Y. Yu, X. Li, A. Simm, et al., "Theoretical model-based quantitative optimisation of numerical modelling for eddy current NDT," *Nondestructive Testing and Evaluation*, vol. 26, no. 2, pp. 129-140, Apr. 2011.
- [17] M. Tanaka and H. Tsuboi, "Finite element model of natural crack in eddy current testing problem," *IEEE Transactions on Magnetics*, vol. 37, no. 5, pp. 3125-3128, Sep. 2001.
- [18] Y. Li, L. Udpa, and S. S. Udpa, "Three-dimensional defect reconstruction from eddy-current NDE signals using a genetic local search algorithm," *IEEE Transactions on Magnetics*, vol. 40, no. 2, pp. 410-417, Mar. 2004.
- [19] F. Jiang and S. L. Liu, "Evaluation of cracks with different hidden depths and shapes using surface magnetic field measurements based on semi-analytical modelling," *Journal of Physics D: Applied Physics*, vol. 51, no. 12, pp. 125002, Mar. 2018.
- [20] C. V. Dodd and W. E. Deeds, "Analytical solutions to eddy-current probe-coil problems," *Journal of Applied Physics*, vol. 39, no. 6, pp. 2829-2838, May 1968.
- [21] T. Theodoulidis and J. R. Bowler, "Eddy-current interaction of a long coil with a slot in a conductive plate," *IEEE Transactions on Magnetics*, vol. 41, no. 4, pp. 1238-1247, Apr. 2005.
- [22] T. P. Theodoulidis and J. R. Bowler, "Eddy current coil interaction with a right-angled conductive wedge," *Proceedings of the Royal Society A: Mathematical Physical and Engineering Sciences*, vol. 461, no. 2062, pp. 3123-3139, Oct. 2005.
- [23] Y. J. Bai, X. Z. Zhang, L. Jiang, et al., "3-D eddy currents analysis in orthotropic materials using truncated region eigenfunction expansion method," *Applied Mechanics and Materials*, vol. 239-240, pp. 258-263, Dec. 2013.
- [24] J. García-Martín, J. Gómez-Gil, and E. Vázquez-Sánchez, "Non-destructive techniques based on eddy current testing," *Sensors*, vol. 11, no. 3, pp. 2525-2565, Feb. 2011.
- [25] B. A. Auld and J. C. Moulder, "Review of advances in quantitative eddy current nondestructive evaluation," *Journal of Nondestructive Evaluation*, vol. 18, no. 1, pp. 3-36, Mar. 1999.
- [26] J. Kim, G. Yang, L. Udpa, et al., "Classification of pulsed eddy current GMR data on aircraft structures," *NDT & E International*, vol. 43, no. 2, pp. 141-144, Mar. 2010.
- [27] C. Voulgaraki, N. Poulakis, and T. Theodoulidis, "Theoretical simulations and quantitative magnetic field measurements for Eddy-current testing with an HTS SQUID system," *IEEE Transactions on Applied Superconductivity*, vol. 23, no. 4, pp. 1603012-1603012, Aug. 2013.
- [28] Maxwell 2D User's Guide, ver. 15, ANSYS Inc., Southpointe, PA, 2012.



Feng Jiang was born in Yancheng, China, in 1981 and received the M.Sc. degree in the School of Mechanical Engineering from Jiangsu University, Zhenjiang, China, in 2006. He is currently pursuing the Ph.D. degree in the School of Mechatronics Engineering and Automation, Shanghai University, Shanghai, China. He is working as an Associate Professor in Mechatronics Engineering at Jiangsu College of Information Technology. His research interests include electromagnetic nondestructive evaluation, sensor techniques and fault diagnosis.



Shulin Liu was born in 1963 and received the M.Sc. degree in the School of Mechanical Engineering from Yanshan University, Qinhuangdao, China, in 1989 and received his Ph.D. degree from Harbin Institute of Technology, Harbin, China, in 2003. Since 2008, he is a Professor and Doctoral Supervisor at School of Mechatronics Engineering and Automation, Shanghai University, China. His major research direction is complex equipment fault diagnosis.